



**HAL**  
open science

# Pore-scale flow measurements at the interface between a sandy layer and a model porous medium: Application to statistical modeling of contact erosion

R. Béguin, P. Philippe, Y.H. Faure

## ► To cite this version:

R. Béguin, P. Philippe, Y.H. Faure. Pore-scale flow measurements at the interface between a sandy layer and a model porous medium: Application to statistical modeling of contact erosion. *Journal of Hydraulic Engineering*, 2013, 139 (1), p. 1 - p. 11. 10.1061/(ASCE)HY.1943-7900.0000641 . hal-00838002

**HAL Id: hal-00838002**

**<https://hal.science/hal-00838002>**

Submitted on 24 Jun 2013

**HAL** is a multi-disciplinary open access archive for the deposit and dissemination of scientific research documents, whether they are published or not. The documents may come from teaching and research institutions in France or abroad, or from public or private research centers.

L'archive ouverte pluridisciplinaire **HAL**, est destinée au dépôt et à la diffusion de documents scientifiques de niveau recherche, publiés ou non, émanant des établissements d'enseignement et de recherche français ou étrangers, des laboratoires publics ou privés.

## **PORE-SCALE FLOW MEASUREMENTS AT THE INTERFACE BETWEEN A SANDY LAYER AND A MODEL POROUS MEDIUM: APPLICATION TO STATISTICAL MODELING OF CONTACT EROSION**

Rémi BEGUIN<sup>1</sup>, Pierre PHILIPPE<sup>2</sup> and Yves-Henri FAURE<sup>3</sup>

<sup>1</sup>LTHE, Université Joseph Fourier, Maison des Géosciences, BP53, 38041 Grenoble, France.  
Email: remi.beguin@gmail.com

<sup>2</sup>IRSTEA, 3275 route de Cézanne, CS40061, 13182 Aix-en-Provence Cedex5, France. Email: pierre.philippe@irstea.fr

<sup>3</sup>LTHE, Université Joseph Fourier, Maison des Géosciences, BP53, 38041 Grenoble, France.  
Email: yhfauere@ujf-grenoble.fr

### **ABSTRACT**

Contact erosion is potentially initiated at the interface between two soil layers by a groundwater flow within the coarser material. Once eroded by the flow, particles from the finer soil are transported through the pores of the coarser layer. Fluvial dykes are often exposed to this phenomenon. Small-scale experiments, combining Refractive Index Matching medium, Planar Laser Induced Fluorescence, and Particle Image Velocimetry, were carried out to measure the flow characteristics in the vicinity of an interface between a model granular medium and a fine graded sandy layer. Longitudinal velocities and shear-stresses distributions were obtained in Darcy flow conditions. They reveal a long tail towards large values which reflects the spatial variability of the constrictions in the pores network. Taking account of these distributions can improve the modeling of contact erosion by going beyond the simple use of mean quantities, like Darcy velocity, as usually proposed in the literature.

## Introduction

Dykes and embankment dams are usually built with several types of materials, each having a particular size distribution associated with a specific function. For example, the core of the structure is impermeable and can be constituted of clay or silt, whereas drains or shoulders are made of coarse sand or gravels. There are consequently many interfaces between materials with different composition which are all potentially subject to internal erosion in the presence of a sufficiently strong groundwater flow. In particular, when these interfaces are in contact with a preferential flow path in a “coarse soil layer”, particles of a “fine soil layer” can be removed and transported through the pores of the coarse layer. This specific type of internal erosion is usually called “contact erosion”. If ever this phenomenon is taking place in a dyke or an embankment dam, severe troubles of the structure are likely and it is therefore a strong demand of dyke stakeholders to better predict and possibly prevent any occurrence of contact erosion according to available data on soil properties.

For contact erosion to be initiated, two conditions must be fulfilled. First, a geometrical condition requires that the smallest sections of the pore network in the coarse soil, also called constrictions, are sufficiently large that the eroded particles can pass through. This condition has been broadly studied, empirically (Sherard, 1984) but also analytically (Locke 2001, Reboul 2010), and reliable criteria have been proposed to predict whether a particle will be able or not to get through a layer of coarse material with a given size distribution. Second, a hydraulic condition reflects the need for a sufficiently strong flow to erode and transport particles. Obviously this second condition applies only when the geometrical one is fulfilled. Several experimental studies were dedicated to this hydraulic condition (Brauns, 1985; Bakker, 1994, Wörman, 1992). All of them postulate that contact erosion can be regarded as conventional surface erosion with the particularity that the flow path is located within a coarse layer. At small scale, inside a pore of a coarse material in contact with the top of a fine soil layer, one recovers indeed a classical situation of surface erosion. Sand erosion has been extensively studied for many decades with significant advances, especially by the introduction of the Shields criterion. An adapted version of this criterion has been proposed for the hydraulic condition of contact erosion (Brauns, 1985, Bakker, 1994), but an empirical factor is needed to coincide with the available experimental data. A law has also been proposed for sand transport capacity by relating the amount of sand transported to the flow characteristics (Wörman, 1992). This law has the particularity to present no hydraulic threshold: sand is transported as soon as flow velocity is not null. The existence of an erosion threshold and the way to express it in empirical or phenomenological erosion laws is a general and debated issue in surface erosion (Lavelle, 1987). In those regimes where erosion is very low, the experimental measurements of a threshold are indeed based on quantitative or visual criteria which are different depending on the authors and which prevent an unambiguous definition of a threshold. Moreover, it has been observed that, when the observation lasts long enough, small quantities of soil can be transported in hydraulic conditions below the conventional threshold that would consequently depend on the patience of the observer. In surface erosion, this phenomenon is usually attributed to time fluctuations of the flow and proposals have been made recently to include them in the definition of an erosion threshold based on impulse instead of shear stress (Valyrakis, 2010).

A statistical approach can be used to account for these temporal variations of the flow properties (Cheng, 2006). In the context of contact erosion, Den Adel proposed such a statistical model by introducing probability distributions for detachment and deposition of the particles (Den Adel, 1994). Nevertheless, he does not consider the spatial fluctuations of the flow stress due to the variability of the pores geometry. Similarly, all the other models of contact erosion predict and quantify the erosion from the mean values of the flow characteristics, thus forgetting the role of spatial heterogeneities encountered by the flow in the coarse layer. Contact erosion is indeed initiated locally, in the zones of highest velocities, and small scale observation of the phenomenon underlines its heterogeneous nature as will be shown in this paper. To account for the spatial variability induced by the pores network, the flow must be characterized at the pore scale.

Contact erosion has been observed experimentally for Darcy velocities from 0.001m/s to 0.1m/s. Coarse layers sufficiently permeable to allow these velocities without unrealistic gradients are constituted of particles with diameter between 1mm and 100mm. In consequence, the Reynolds number of the flow, calculated with particles diameter and Darcy velocity, ranges from 10 to  $10^4$ . In terms of porous flow regimes (Bear, 1972), viscous forces are dominant until  $Re=1$  to 10 and Darcy law applies. Above  $Re=10$ , inertial forces are no more negligible and several empirical laws, as Forchheimer's one, can account for them. Temporal variations of the flow start at  $Re=80$  to 120 and turbulent regime is finally reached at  $Re=300$  to 600 (Hlushkou, 2006). So, contact erosion is usually initiated in a Forchheimer flow regime where both viscous and inertial forces must be considered.

Measurements of flow characteristics at pore-scale have been realized by Nuclear Magnetic Resonance methods (Lebon, 1996; Johns, 2000) and by Laser Doppler Velocimetry (Giese, 1998) or Particle Tracking Velocimetry in a refraction-index matched porous medium (Rashidi, 1996; Lachhab, 2008; Huang, 2008). Numerical simulations have also been carried out by Lattice Boltzmann method (Maier, 1999) and by direct resolution of Navier-Stokes equations (Magnico, 2003). All these experimental and numerical techniques provide velocity fields of the flow at the pore-scale. The velocities distributions have been computed and show, in almost all the cases and for many different values of Reynolds number, that the velocity component in the main flow direction is approximately distributed according to a log-normal law whereas the transverse component distribution is centered on 0.

The present study is motivated by such flow measurements at the pore scale in the context of contact erosion where a layer of fine particles is lying under a porous medium. Particle Image Velocimetry (PIV) measurements by Planar Laser Induced Fluorescence (PLIF) in a Refraction-Index Matched (RIM) medium made of glass beads have been carried out in the vicinity of the interface between the porous layer and an underlying sandy layer. The paper is organized as follows. The experimental set-up as well as the Image Processing and PIV methods are detailed in section 2. The experimental results are presented in section 3: porosity and mean longitudinal velocity component profiles over the interface, 2D velocity field, distributions of transverse and longitudinal velocity, shear-stress 2D field and distribution. Section 4 illustrates how the understanding of previous results on contact erosion (Beguin) can be improved by a probabilistic approach that takes into account the spatial variability of the pores network through the use of the experimental shear-stress distribution. Conclusions and prospects are discussed in the last section

## 2 Experimental set-up and optical techniques

### 2.1 Set-up

To achieve pore scale velocity measurements at an interface between a coarse porous medium and a sand layer, we have used a Refractive Index Matching medium to allow direct visualization of the porous flow. This medium is constituted of spherical borosilicate beads, manufactured by SiLi®, which are immersed in a mixture of two mineral oils in proportions such that the refractive index of the liquid is matched to that of the borosilicate glass  $n \approx 1.473$ . This matching makes the medium translucent and allow for visual observation through the porous medium. This model porous medium is placed over a layer of sand inside a rectangular plexiglass box with internal dimensions 80 x 80 x 400 mm. The sand layer is realized by filling half height of the cell with NE34 sand from SIBELCO®. It is a well-graded sand with  $D_{50} = 204 \mu\text{m}$  and  $Cu = 1.5$ . To obtain a perfectly saturated layer without any air bubbles, the sand is directly poured in the oil at small flow rate. Once it has completely settled down, it is slightly compacted but remains very loose. Borosilicate beads are then placed above the sand layer. Note that the first layer of beads partially sinks into the poorly consolidated sand. To prevent ordered arrangements of the beads at the wall which would generate preferential flow path, a bimodal size distribution was used: 50% of beads with  $d = 9.7 \text{ mm}$  and 50% of beads with  $d = 7.3 \text{ mm}$ . The mean bead diameter is  $\hat{d} = 8.5 \text{ mm}$ .

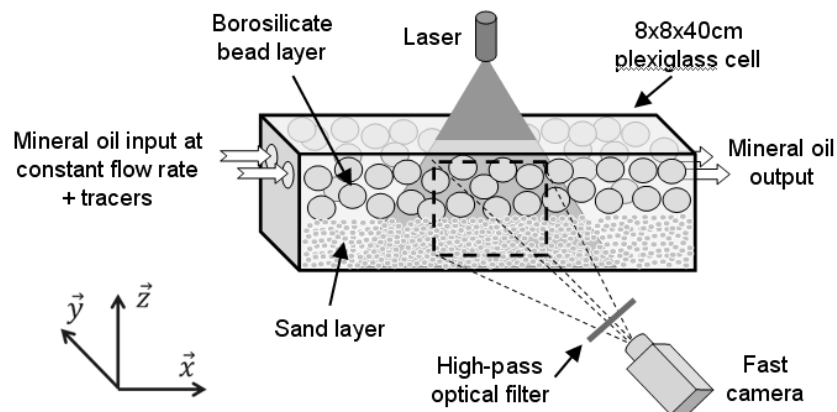
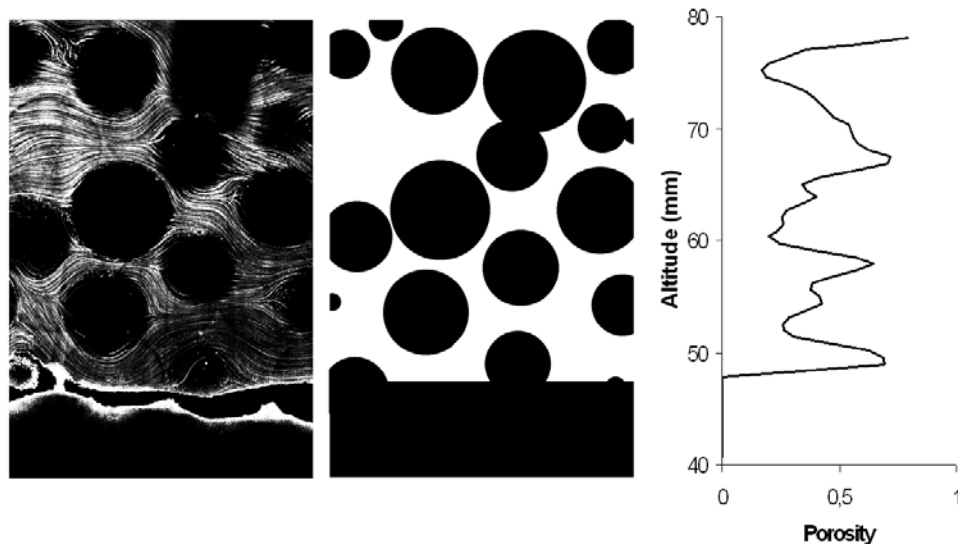


Fig. 1 Sketch of the experimental device developed for pore scale flow measurements.

The objective of these experiments is to measure locally the velocity field of the flow in the vicinity of the interface between sand and porous layer and to characterize the stress induced by the flow on the sand which can initiate contact erosion. To this end, a small amount of fluorescent tracers is seeded in the oil mixture and a flow at constant flow rate is generated into the porous layer by a gear pump. These tracers have a negligible settling velocity compared to the characteristic velocity of the flow and can therefore be considered as passive tracers. A green laser line generator module is fixed above the cell and illuminates the Refractive Index Matched medium in a vertical plane, parallel to the flow direction, which has

a triangular shape with a fan angle of  $60^\circ$ , a uniform intensity distribution, and a small width a priori lower than 0.5 mm. The tracers, whose fluorescence is activated in the plane illuminated by the laser at 532 nm, reemit at higher wavelengths. Then, by interposing a high-pass optical filter at 590 nm, only the tracers located in the plane generated by the laser are visible while all reflections due to the direct laser emission are eliminated. The position of the light plane can be varied longitudinally and transversely inside the cell. For a given configuration of the plane, the positions of the tracers are recorded with a high-speed camera (Fastcam SA3, Photron), at 125 fps and with a resolution of 1024 x 1024 pixels, in an area of approximate dimensions 25 x 25 mm. Spatial resolution per pixel is therefore about 24  $\mu\text{m}$ . A sketch of the experimental device is shown in Fig. 1.

Each experiment is realized as follows. First, a measurement zone is selected in the middle of the cell in the longitudinal direction. The location of the measurement area is achieved by transversal translation of the Laser sheet relative to the cell. Series of 500 images are recorded at regular spacing of 2.5 mm in the half-thickness of the cell. The 500 image series are composed of 10 sequences separated by 2 seconds; each sequence being composed of 50 images recorded at 125 fps.



**Fig 2.** Addition of 500 images (left); Mask deduced from the Image Processing algorithm (middle); Vertical porosity profile (right).

## 2.2 Image Processing for porosity measurement

In each measurement area, Image Processing allows to identify grains with respect to the liquid phase. To this end, all the pictures are added. Then, by identifying the dark areas with discs in the resulting image, a binary mask is obtained. The porosity vertical profile is then calculated at each horizontal line. Fig.2 shows an example of a binary mask and of the computed vertical profile of porosity.

## 2.3 Particle Image Velocimetry

For each acquisition, the mean background is subtracted to all the pictures so as to visualize only the mobile tracers as can be seen in Fig.3.a. Then, 2D displacement fields of the tracers are calculated by Particle Image Velocimetry processing, performed on each of the 250 couples of successive frames, using the software DPIVsoft developed by Meunier et al. (Meunier, 2003). As time interval between two frames is 8ms, one gets finally the 2D velocity fields with an approximate spatial resolution of one vector every 0.4 mm. Since the maximum Reynolds number measured is  $Re = 10$ , the flow is stationary without any time fluctuations. However, such fluctuations are observed in the raw fields and can be attributed to PIV errors due to a lack of homogeneity of the tracers and mostly to the transversal flow which is far not negligible owing to the intrinsic tortuosity of the porous medium. To minimize the impact of these errors, the 250 velocity raw fields obtained for one measurement zone are averaged. Indeed, we have checked that such a time averaging of the velocity fields does not smooth the existing spatial fluctuations while reducing considerably the noise. Finally, the binary mask presented in section 2.2 is applied to the average velocity field so as to impose exactly a zero velocity contribution in the areas where there is no liquid. A typical 2D velocity field is shown in Fig.3.b.

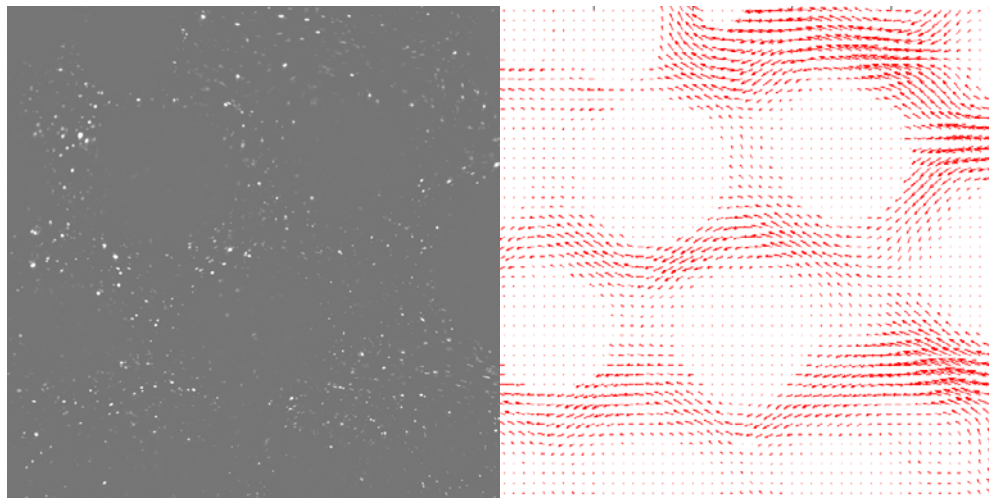


**Fig 3.** Typical image of the fluorescent tracers (left); Corresponding velocity field (right).

## 3 Results

### 3.1 Velocity

#### a. Velocity fields

The mean velocity field (Fig.3.b) obtained with the previously described experimental set-up and data processing is the starting point of the following analysis. A first qualitative

observation of these fields highlights classical characteristics of porous flow at pore scale with a sharp spatial velocity distribution in both direction and magnitude (Hlushkou, 2006). The pore network where the flow develops can be seen as large voids, created by the existing space between several grains in contact, connected one to another by narrow sections, called constrictions. As can be seen in Fig.4, from a void, the flow converges to a constriction, accelerates due to the reduction of the section and then diverges and slows down into the following void. These voids are places of both flow separation through different constriction outlets and flow mixing from different constriction inlets. It can also be noted that the velocity intensities are higher in some pores (see for instance in the middle left part of the field shown in Fig.4). This can be attributed to the presence of a larger void, to a local reorientation of the transverse flow, or to a direct alignment of successive constrictions. Focusing on velocity into the section of a constriction, one can notice that velocity magnitude is maximal close to the center of the section and decreases on both sides until reaching very low values at the beads interface. This is typical of a Poiseuille flow profile.

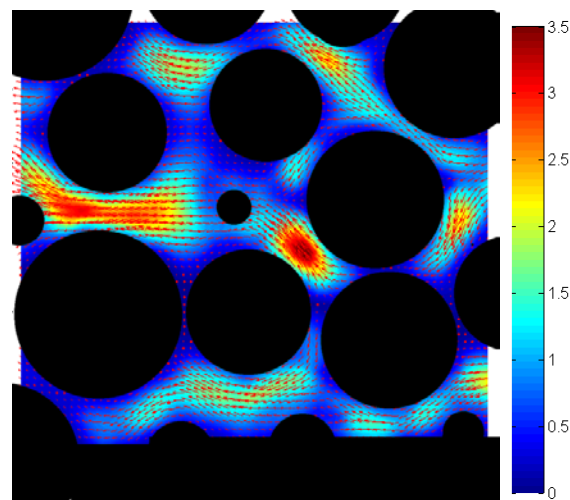


**Fig 4.** Velocity vectors field (red arrows) and velocity magnitude map (color level scale in mm/s).

#### b. Mean Velocity profile

Mean velocity profiles have been computed by averaging the horizontal and vertical components over each horizontal row of the velocity field. The masked area of the velocity field, which correspond to the beads positions, are included in the calculation and these velocity profiles correspond therefore to the bulk velocity which, averaged on a larger Representative Elementary Volume, would give the so called Darcy Velocity. The mean pore velocity has also been calculated considering only the pores spaces (i.e. not masked). Then, these profiles have been averaged over the seven vertical areas of measurements, spaced apart by 2.5 mm in the transverse direction.

The resulting mean velocity profiles are shown in Fig.5 together with the porosity profile calculated as described in chapter 2.2 and spatially average in a similar manner than the velocity. The vertical distance to the sand top surface has been normalized by the bead mean diameter  $\hat{d} = 8.5mm$ . Owing to the permeability contrast between the beads and the sand



layer, the velocity in sand is supposed to be negligible and is not measurable anyway since the tracers are no longer visible in the sand layer. As can be seen in Fig. 5, above the interface, the velocities increase rapidly into the bead layer. Then, the bulk velocity fluctuates around a mean value of about 1.4 mm/s. These large fluctuations are linked to the local organization of the beads, more or less in successive layers. Indeed, a correlation between the calculated velocity profiles and the porosity profile can be observed in Fig.5. The influence of the boundary layer on the velocity profile is limited to a small extent above the sand interface, about half a bead diameter. Given that erosion is initiated in this contact zone, we find that the mean velocity in the porous layer does not accurately reflect the actual local flow likely to pull out sand grains. Note finally that, as expected, the bulk vertical velocity is almost zero.

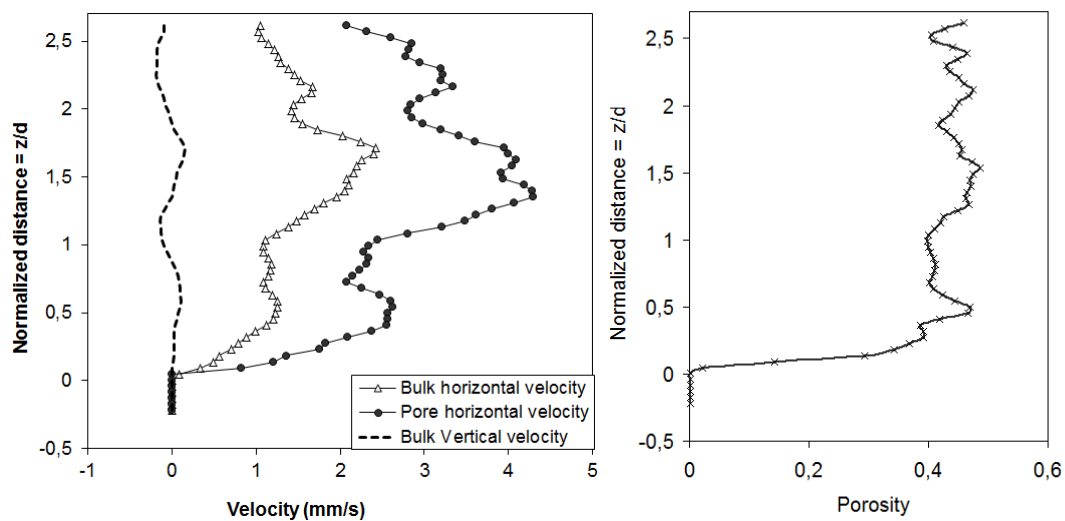


**Fig 5.** Vertical profiles of the different mean velocities (left) and of porosity (right).

### c. Velocity distributions

The mean velocity profiles provide only part of the information by averaging the very large local variations of the velocity observed in the porous flow. To capture this spatial variability, statistical velocity distributions have been computed from all the flow fields measured. The probability density functions of the normalized vertical and horizontal components are represented in Fig.6 together with previous results from numerical simulations (Magnico, 2003) and from experiments (Cedenese, 1996; Lebon, 1996). The statistical distribution of the vertical component of velocity has been normalized by the mean horizontal component as the mean vertical one is almost zero. Both vertical and horizontal distributions are in very good agreement with the previous numerical and experimental results. The horizontal component distribution is characterized by very low probabilities for negative values, a peak at a quite small positive value and a large tail that spreads until relatively large positive values. This means that large values of the local velocity exist, even for a small value of the mean velocity. The standard deviation of the distribution is  $\sigma = 1.9$ , and the probability to have a local value 5 times larger than the mean velocity is about 5%. On the contrary, the vertical component distribution is symmetric, with a peak value and a sharp steep change at zero. The mean value of the vertical component is about 1% of the

mean value of the horizontal component, confirming that there is no global vertical flow. The mean of the absolute value of the vertical component is 0.68 mm/s which correspond to about 50% of the mean horizontal component magnitude. These measurements are only 2D but the third component, in the transverse direction  $y$ , can be reasonably assumed to be distributed in a similar manner than the vertical component.

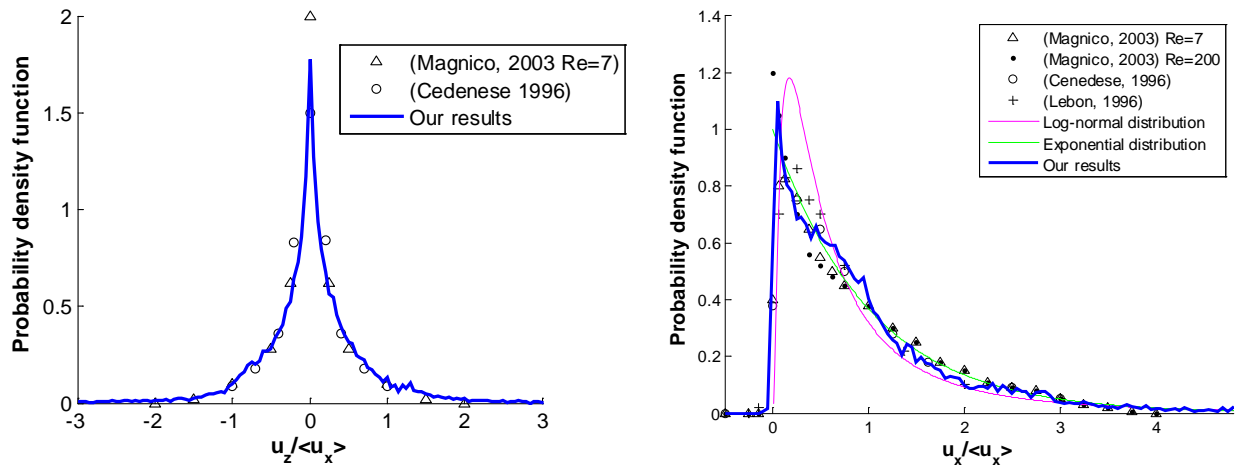


**Fig. 6.** Probability density functions of vertical (left) and horizontal (right) component of velocity.

### 3.2 Shear-stresses

Since the porous flow regime is purely viscous in the experiments and since our oil is a Newtonian fluid, the horizontal shear-stress along the main flow direction (i.e.  $x$ ) into the liquid phase is simply given by the following formula (with the directions  $x$ ,  $y$  and  $z$  given in Fig.1):

$$\tau_{xz} = \mu \frac{\partial u_x}{\partial z} \quad (1)$$

Note that, as our device only allows for 2D velocity fields in vertical planes, the second component of the shear-stress exerted by the flow, namely  $\tau_{yz}$ , can not be evaluated. Although the  $x$ -direction corresponds to the main direction of flow, the tortuosity of the porous medium induces a contribution the transverse velocity gradient which is certainly significantly lower than the longitudinal velocity gradient but still not negligible.

An example of the horizontal shear-stress field computed directly by derivation of the velocity field in Fig.4 is presented in Fig.7. As can be seen, the highest absolute values of the

shear-stress are located in constrictions but the maximal values are not exactly located at the bead surface as they should. This point is discussed just below.

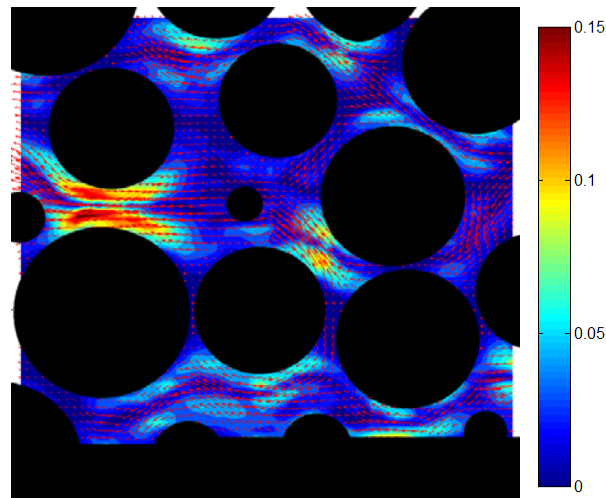


**Fig. 7.** Velocity vectors field (red arrows) and shear-stress magnitude map of  $\tau_{xz}$  (color level scale in Pa).

In the context of contact erosion, shear-stress in the vicinity of sand layer surface is of great interest since it will control erosion of sand (Ariaturai, 1978; Bonelli, 2006). In consequence, a specific analysis of the horizontal shear-stress is made at the interface between sand and water in neighboring pores. Typical horizontal velocity and shear-stress profiles in one pore located just above the sand layer are presented in Fig.8.

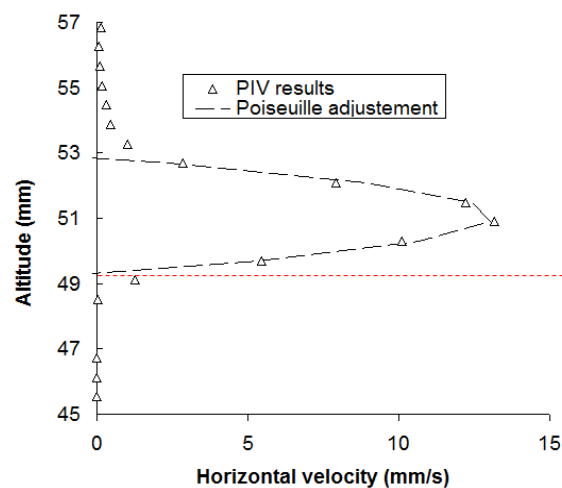


**Fig. 8.** Velocity profiles along a vertical section in a pore located at the sand upper surface.

As can be noticed, the velocity profile is in relatively good agreement with the Poiseuille's law that accounts for the velocity profile between two walls in laminar flow regime:

$$u_x(z) = u_{\max} \left( 1 - \frac{4z^2}{h^2} \right) \quad (2)$$

with  $u$  the velocity,  $z$  the vertical position (i.e. distance from the midplane),  $u_{\max}$  the maximal velocity at the center of the pipe, and  $h$  the gap between the two walls. From equation (2), the following expression is obtained for the shear-stress at the lower wall:

$$\tau_{xz} \left( z = -\frac{h}{2} \right) = \frac{4\mu u_{\max}}{h} \quad (3)$$

It can be seen from Fig.8 that the experimental data diverge from Poiseuille's prediction when reaching the top of the pore. This can be attributed to both explanations: 1) the exact geometry of the tortuous pore that differs from a constant gap; 2) the PIV interrogation boxes which, near the top of the pore, are filled simultaneously by a fixed part corresponding to the upper bead and by mobile tracers and induce a smoothing of the velocity profile. This effect is much less visible at the bottom of the pore but does not allow pinpointing precisely the position of the interface. Hence, the direct calculation of the bottom shear-stress at the interface from derivation of the velocity field according to Eq.(1) as presented in Fig.7 is not sufficiently accurate and should be discarded, especially in the vicinity of the sandy interface. An alternative way to estimate the bottom shear-stress is to use an adjustment of the Poiseuille's law given by Eq.(2) and, from the values obtained for the two parameters  $u_{\max}$  and  $h$ , to evaluate  $\tau_{xz}$  thanks to Eq.(3). This adjustment is performed solely in the center part of the flow and only the values of the bottom shear-stress calculated with at least 3 points of the velocity profile and with a coefficient of determination of the fit  $R^2$  superior to 0.8 have been considered. The interface position is obtained as the lower root of the adjusted parabola. Thank to this method, the PIV velocity values close to the interface which are suspected to be biased are not used. Moreover, the position of the sand interface has not to be identified on the recorded images but can be deduced from the Poiseuille's adjustment on the velocity profile which avoids any error in the interface identification due to the presence of sand in-between the studied section and the camera. An example of shear-stress values obtained at a sand interface with this procedure is presented in Fig. 9.

This method can be generalized in the whole porous layer with regularly spaced vertical sections in all the pores. The corresponding normalized statistical distributions of the shear-stresses are shown in Fig 10

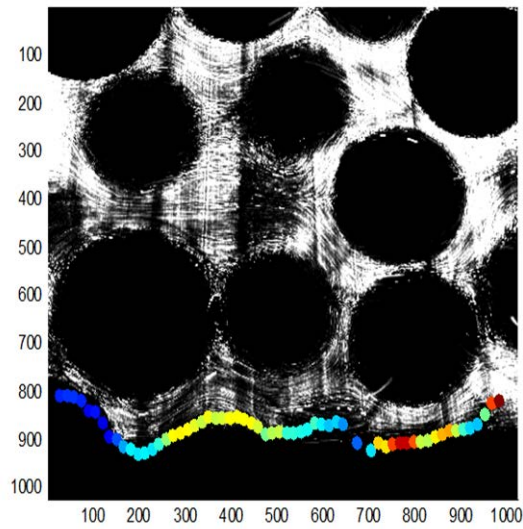


Fig. 9. Shear-stress values estimated along the sand surface (color level scale in Pa).

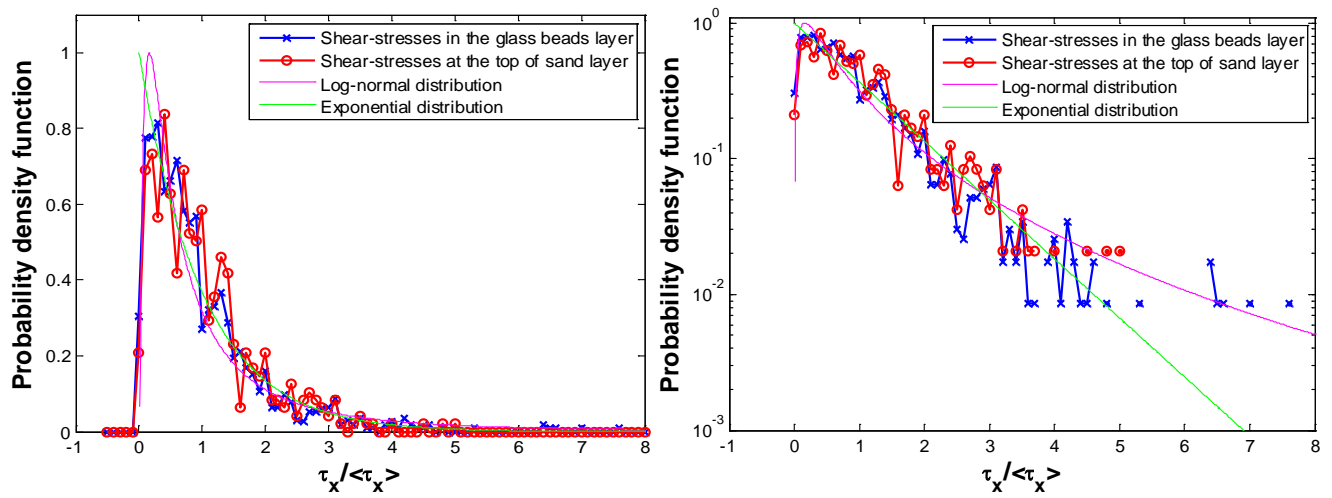


Fig. 10. Shear-stress distributions inside the porous medium and at the sand interface in both linear (left) and logarithmic (right) representation.

These curves are very similar to the ones obtained for the horizontal components of velocity but with much more noise due to the smaller quantity of values used for the calculation of the statistical distribution (17000 velocity values but only 500 shear-stress values). The only difference is the mean value  $\langle \tau_{xz} \rangle$  of the shear-stress distribution which is higher in the glass bead bulk than when the calculation is restricted to the zone in contact with the sand layer :  $\tau_{Bulk} \approx 0.152 Pa$  versus  $\tau_{Interface} \approx 0.068 Pa$ . This difference can be explained by the higher pore flow velocity measured inside the porous medium than just above the interface (see for instance Fig.5.).

As for velocity, these shear-stress distributions are compatible with either a log-normal or an exponential law. Nevertheless, for high values of the normalized shear-stress, an exponential law seems to better reproduce the measurements as can be seen in Fig.10. For instance, the standard deviation of the distribution in the porous medium is  $\sigma_{Bulk} \approx 0.155 Pa$ , very close to the mean value of 0.152 Pa as is expected for an exponential distribution. The same holds for the distribution at the sand interface. In the end, these distributions have a large tail: locally, high values of shear-stress are possible even for low mean value, and the probability to find a local value 3 times larger than the mean one is about 5%. This has important implications for the erosion process to be discussed in the next chapter.

## 4 Towards statistical modeling of contact erosion

### 4.1 Comparison between measurements and analytical relation to estimate mean shear-stress in a porous medium.

Contact erosion appears when a flow through a coarse soil layer is able to pull out particles from the surface of a fine soil layer in contact. At the coarse layer pore scale, this process is very similar to usual surface erosion. Therefore, in order to model contact erosion, several authors have chosen to adapt surface erosion laws established for riverbed erosion. These laws usually consider that hydraulic shear-stress as the adequate variable to represent hydraulic loading on a sediment bed. The key point to adapt fluvial erosion laws to contact erosion is to determine the hydraulic shear stress at the interface as a function of macroscopic values that can be measured experimentally or estimated (mean gradient, mean velocity).

Two different analytical expressions have been identified in the literature to calculate the mean shear-stress into a porous medium.

First, Reddi et al. (Reddi, 2000) proposed a relation based on a capillary tube model of porous medium. An assembly of tubes is considered, with radii chosen to provide the same global permeability than the initial porous medium, assuming a Poiseuille (laminar) flow into each tube. The number of tubes per volume unit is selected to conserve porosity. Then, in this model porous medium, a mean shear-stress at the solid liquid interface can be calculated from the global hydraulic gradient  $i$  (m/m), the intrinsic permeability of the medium  $k$  (m<sup>2</sup>), the porosity of the beads layer  $n$  and the density of the liquid  $\rho_w$  (kg/m<sup>3</sup>):

$$\tau_R = \rho_w g i \sqrt{\frac{2k}{n}} \quad (4)$$

Second, Wörman et al. (Wörman, 1992) obtained a different expression when expliciting the mechanical equilibrium between head-losses in the porous medium and shear-stress at the solid-liquid interface:

$$\tau_W = n \rho_w g i \frac{1}{A_s} \quad (5)$$

with  $A_s$  (1/m) the specific surface of the porous medium. This specific surface can be linked to the intrinsic permeability of the medium in the case of spheres assembly, by the Kozeny-Carman relation (Bear, 1972):

$$k = \frac{c_o \cdot n^3}{A_s^2} = \frac{c_o \cdot n^3 d^2}{36(1-n)^2} \quad (6)$$

with  $c_o$  the Kozeny-Carman coefficient, usually taken equal to 0.2.

Combining relations (4), (5) and (6) it is easily found that the two expressions of the mean shear-stress are directly related (assuming  $c_o = 0.2$ ):

$$\tau_R = 0.63 \times \tau_W \quad (7)$$

These expressions can now be compared to our measurements presented above in section 3. A mean shear-stress value of  $\langle \tau_{xz} \rangle_{Bulk} = \tau_{Bulk} = 0.152 Pa$  was obtained at the liquid/solid interface in the porous bulk of beads. In this test, the global porosity of the bead layer is  $n = 0.43$ , calculated by dividing the total mass of glass beads by the volume of the cell. But, far enough from the boundary limits, the real porosity inside the porous medium is  $n = 0.37$ , a value deduced from a relation due to Ben Aïm which accounts for side effects (Ben Aïm, 1970). From PIV measurements, the mean Darcy velocity is  $U = 1.62$  mm/s while the intrinsic permeability can be calculated from equation (6) with:  $k = 4.9 \times 10^{-8} m^2$ . With these data, the hydraulic gradient  $i$  is deduced from Darcy law,  $U = (k \rho_w g / \mu) \cdot i$ , to be equal to  $i = 0.072$  m/m. This value is consistent with the one measured experimentally during the test:  $i = 0.082$  m/m. It is now possible to evaluate the mean shear stress predicted by the two analytical relations previously mentioned. The corresponding values are listed in Table 1 and compared to our measurements.

	$\langle \tau_{xz} \rangle$
Expression (4) (Reddi, 2000)	0.311 Pa
Expression (5) (Wörman, 1992)	0.491 Pa
Measurement in bead layer	0.152 Pa
Measurement at sand surface	0.068 Pa

**Table 1.** Comparison of two analytical expressions of the mean shear-stress with our measurements.

The analytical expressions from Reddi and Wörman overestimate our measurements in the bead layer respectively by a ratio of about 2 and 3. Part of this discrepancy can be attributed to the fact that, with our 2D velocity fields, our measurements of the mean shear-stress are limited to the  $\tau_{xz}$  component to the detriment of the  $\tau_{yz}$  component. However, as already discussed in the previous section, the contribution of the missing component is less than the other one and, consequently, this can not account for such a ratio between analytical expressions and measurements. This should be explained more likely by the fact that the proposed theoretical expressions are incorrect in our case, probably because the assumptions they derive are too restrictive.

More experiments should be necessary to validate this explanation with a broader comparison. Nevertheless, in a first step, we proposed to make a rough estimation of the shear-stress in the bead layer with the available data. To this end, Wörman relation is used, but corrected with an empirical factor:  $\beta_w = \frac{\tau_{Bulk}}{\tau_w} \approx 0,3$  to match with our bulk measurement.

This coefficient would slightly increase if it were possible to consider the second component in the calculation of the mean shear stress but it would nevertheless remain well below 1.

Another important result that can be noticed in Table 1 and that was already reported in section 3, is the discrepancy between the mean shear-stress in the bead layer and at the sand surface. This is a purely geometrical effect due to flow in porous medium which is significantly different in the middle of the medium and at its borders. As a consequence, we suggest to use another correction factor to relate bottom shear stress at the interface to porous

bulk shear stress:  $\beta_i = \frac{\tau_{Interface}}{\tau_{Bulk}} \approx 0,5$ .

The values of these two empirical parameters should be validated by other experiments. In particular, the parameter  $\beta_i$  is certainly a function of grain arrangement at the interface. Its initial value may vary with the protocol used to construct the two layers. More, even for a given protocol, erosion and transport of sand grains will progressively modify the interface and thus change the  $\beta_i$  value. A specific study should be conducted on this aspect.

## 4.2 Stochastic model for contact erosion

### a) Analytical expression of the global erosion law

As underlined previously, high shear-stress values can be achieved locally even for a low mean value. In consequence, to correctly model contact erosion process, it is necessary to consider the whole distribution of longitudinal shear-stress components rather than only the mean value. A very realistic assumption in the light of experimental results is to use an exponential law for this distribution. Although the experimental distributions have been obtained in the specific configuration of a bidisperse glass bead medium, at low Reynolds number, we assume in the following that the shape of the distributions remains unchanged for



higher Reynolds number and for other porous medium geometries. This assumption may not be valid in some situations but, in a first step, it makes possible a simple analytical calculation for contact erosion process. The local bottom shear stress  $\tau$  is therefore given by the following statistical distribution with the mean bottom shear stress  $\langle \tau \rangle$  as the only parameter:

$$f(x) = \frac{1}{\langle \tau \rangle} e^{(-x/\langle \tau \rangle)} \quad (8)$$

It should be noted that introducing a spatial distribution of shear stresses is mathematically similar to models based on a temporal distribution of shear stresses in a turbulent flow (Van Prooijen, 2010; Duan, 2010).

To account locally for erosion at the sand surface, a classical linear excess shear stress law is used:

$$\varepsilon = \begin{cases} k_{er}(\tau - \tau_c) & \text{if } \tau > \tau_c \\ 0 & \text{otherwise} \end{cases} \quad (9)$$

with  $\varepsilon$  the local erosion rate (kg/s/m<sup>2</sup>),  $\tau_c$  the critical shear stress for erosion initiation (Pa),  $\tau$  the shear-stress exerted locally by the flow at the surface of the eroded material (Pa) and  $k_{er}$  a coefficient of erosion (s/m). This relation is the simplest one can imagine to mimic erosion above a threshold. Its validity has not been physically proved and is often discussed, but the expression is widely used for fine soil erosion, and is in good agreement with lot of dataset (Ariathurai, 1978; Knapen, 2007).

The global erosion rate is calculated by summing the erosion rate in all areas where erosion occurs, i.e. everywhere where the local bottom shear stress  $\tau$  is greater than the critical shear stress  $\tau_c$ :

$$\langle \varepsilon \rangle = \int_{\tau=\tau_c}^{+\infty} f(\tau)k_{er}(\tau - \tau_c)d\tau = k_{er} \langle \tau \rangle \exp\left(-\frac{\tau_c}{\langle \tau \rangle}\right) \quad (10)$$

One of the most important consequences of equation (10) is the disappearance of the threshold as soon as global quantities are considered. This is quite important for small mean shear stress values, especially below the critical threshold ( $\langle \tau \rangle < \tau_c$ ), where there exists a very low but not null erosion inside a sufficiently large sample. Conversely, for high values of the mean shear stress, one recovers a linear relation between global erosion rate and mean shear stress, similarly to the local erosion law.

Next step of our stochastic model is to account for the variability of the critical shear stress. Indeed, as underlined by various authors, each grain submitted to erosion has a different resistance, even for a model homogeneous material with uniform type of grains. In this specific case, only the geometrical disposition of the grains can provide some variability to their resistance, the grains fully exposed to the flow being more easily removed than the ones hidden by their neighbours (Cheng, 2002). Now, if a polydisperse material is considered, the size of the grains will provide another source of variability and, for a real granular soil, the shape of the grains will also vary from one to another and consequently enhance or decrease sensibility to erosion. Finally if one is not restricted only to granular soils, other processes of

chemical, biological, or electrical origin will generate adhesion forces between grains that will depend on many factors and will vary locally at the soil surface. In consequence, a statistical distribution for the grain resistance to erosion is needed to represent all the previous listed parameters which are sources of variability. In a first approximation a normal distribution will be used. As negative values of critical shear-stress have no physical meaning, the normal distribution is truncated below 0 Pa:

$$g(\tau_c) = C_g \frac{1}{\sigma_{\tau_c} \sqrt{2\pi}} \exp\left(-\frac{(\tau_c - \langle \tau_c \rangle)^2}{2(\sigma_{\tau_c})^2}\right) \quad \text{if } \tau_c > 0 \quad (11)$$

$$g(\tau_c) = 0 \quad \text{if } \tau_c < 0$$

with  $C_g = \left(1 - \text{erf}\left(-\frac{\langle \tau_c \rangle}{\sqrt{2}\sigma_{\tau_c}}\right)\right)^{-1}$  a coefficient needed to normalize the truncated distribution.

Implementing this expression into the erosion law provides the following relation:

$$\langle \varepsilon \rangle = \int_0^{+\infty} \int_{\tau=\tau_c}^{+\infty} f(\tau) k_{er} (\tau - \tau_c) d\tau_c d\tau = \int_0^{+\infty} k_{er} g(\tau_c) \langle \tau \rangle \exp\left(-\frac{\tau_c}{\langle \tau \rangle}\right) d\tau_c \quad (12)$$

By the change of variable  $X = \frac{\tau_c - \langle \tau_c \rangle}{\sigma_{\tau_c}} + \frac{\sigma_{\tau_c}}{\langle \tau \rangle}$ , one gets finally for the global erosion rate:

$$\langle \varepsilon \rangle = C_g k_{er} \langle \tau \rangle \exp\left(-\frac{\langle \tau_c \rangle}{\langle \tau \rangle} + \frac{\sigma_{\tau_c}^2}{2\langle \tau \rangle^2}\right) \left(1 - \text{erf}\left(\frac{\sigma_{\tau_c}}{\sqrt{2}\langle \tau \rangle} - \frac{\langle \tau_c \rangle}{\sqrt{2}\sigma_{\tau_c}}\right)\right) \quad (13)$$

It is also possible to choose, instead of a truncated normal distribution, a uniform distribution for the critical shear-stress of density:  $h(x) = 1/2 \cdot \sigma_{\tau_c}$  in the range  $[\langle \tau_c \rangle - \sigma_{\tau_c}; \langle \tau_c \rangle + \sigma_{\tau_c}]$ . This distribution is rather unrealistic but enables a straightforward study on the influence of the width of the distribution. The global erosion rate is now given by:

$$\langle \varepsilon \rangle = k_{er} \langle \tau \rangle \exp\left(-\frac{\langle \tau_c \rangle}{\langle \tau \rangle}\right) \left(\frac{\text{sh}\left(\frac{\sigma_{\tau_c}}{\langle \tau \rangle}\right)}{\frac{\sigma_{\tau_c}}{\langle \tau \rangle}}\right) \quad (14)$$

In Fig.11, we have plotted the local erosion rate given by equation (9) together with the different expressions of the global erosion rate obtained for an exponential distribution of bottom shear stress and for punctual, normal truncated, and uniform distribution of critical shear stress. A dimensionless representation is used to make easier the comparison between the different curves.

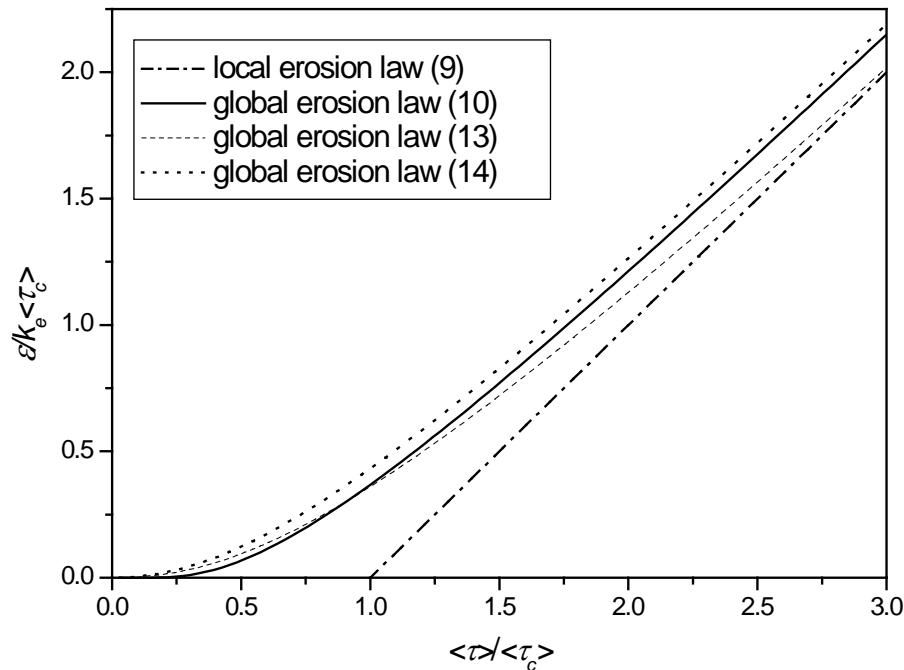


**Fig. 11 :** Dimensionless erosion rate versus dimensionless mean shear stress calculated for the local erosion law given by equation (9) (dash-dotted line) and for the global erosion law obtained with an exponential distribution of shear stress, and for different statistical distributions of critical shear stress: punctual (plain line), truncated normal (dashed line), and uniform (dotted line). The two last distribution have been chosen with a very large normalized standard deviation:  $\alpha = \sigma_{\tau_c} / \langle \tau_c \rangle = 1$ .

As already mentioned above, the statistical distribution of shear stress eliminates the existence of threshold. The mean erosion rate is no longer a linear function of the excess shear-stress except in the range of large mean shear stress which is not much relevant in the context of erosion in a dyke where the kinetics of erosion is very slow. On the other hand, introduce a statistical distribution of critical shear-stress has a very weak influence of the global law, even for a large standard deviation ( $\alpha = \sigma_{\tau_c} / \langle \tau_c \rangle = 1$ ) as can be seen in Fig.11.

To conclude, the main consequence of this stochastic approach to contact erosion is that there is no longer an erosion threshold which provides a practical limit not to cross and give the guarantee that erosion will not develop. On the contrary, erosion can occur as soon as the shear-stress is not null. This influence of the statistical distribution of the loading is a plausible explanation on the difficulty to establish a definition of a threshold (Lavelle, 1987). This is also a possible source of uncertainty on the experimental measurement of  $\langle \tau_c \rangle$  and  $k_{er}$ . For example, in Fig.12, some arbitrary measurement values have been plotted on the global law calculated for an exponential shear stress distribution and a punctual distribution of resistance. If a linear law is fitted on these experimental data, a 41% error is made on the estimation of  $\langle \tau_c \rangle$ , and a 12% error on the value of  $k_{er}$ .

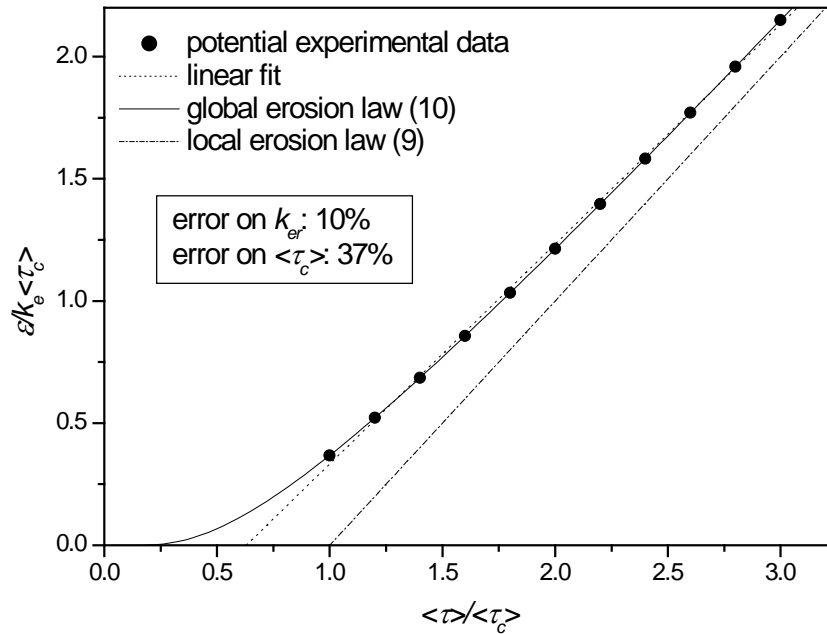


**Fig. 12 :** Typical errors on  $\langle \tau_c \rangle$  and  $k_{er}$  when the local erosion law is used to fit experimental data for global erosion rate.

#### b) Stochastic model, temporal evolution

It has been experimentally observed that the erosion rate measured when soils are submitted to contact erosion evolves with time (Guidoux, 2010). The global tendency identified is an exponential-like decay of the erosion rate. Coherently with the previous conclusion on the disappearance of the threshold by spatial averaging, small erosion rates are measured even for very low mean shear-stress (or velocity), but these erosion rates rapidly decrease with time, until going back to zero or at least below turbidimeter measurement accuracy. Indeed, as can be observed in Fig.13, when the mean velocity is increased into the porous medium, a “peak” of turbidity is first measured, followed by a progressive decrease. Water turbidity is quantitatively related to the quantity and the characteristics (shape, colour...) of the particles transported by the flow. In a first approximation, it is simply proportional to the soil suspension concentration in the flow (Guidoux, 2010).

The decrease with time of the erosion rate after a peak can be explained by hardening of the eroded soil surface due to segregation: the weakest particles are more easily removed by the flow and, consequently, the proportion of grains with a high erosion resistance increases significantly at the surface. This is a classic observation for river bed erosion (Hunziker, 2002).

This phenomenon of sorting at the eroded surface is not included in the stochastic model proposed above and we will therefore seek to enrich it so as to model also this effect. The final model is detailed below in a purely stochastic version (Monte Carlo type) as the direct analytical solution is no longer possible.

First, to represent the variability of the flow loading, a large number  $N$  of shear-stresses is randomly picked up in the statistical distribution of shear-stress given in equation

(8). Each shear-stress value  $\tau_i$  is associated with a resistance to erosion represented by a critical shear-stress  $(\tau_c)_i$  and a coefficient of erosion  $(k_{er})_i$ . For simplify,  $k_{er}$  is considered as constant while  $\tau_c$  values are distributed according for instance to a log-normal law truncated below 0. At each time step, tanks to the local erosion law in equation (9), a local erosion rate  $\varepsilon_i$  is calculated for each couple of hydraulic shear stress  $(\tau_i)$  and soil resistance  $((\tau_c)_i, (k_{er})_i)$ . The global erosion rate is then given by:  $\langle \varepsilon \rangle = \sum_{i=1}^N \varepsilon_i / N$ . At this level, we have checked that this stochastic model is strictly equivalent to the analytical expression in equation (13) as soon as  $N$  is sufficiently large (roughly  $N > 10^5$ ).

Then, to model the temporal evolution of the erosion rate, we now allowed the resistance to evolve during the process of erosion if a sufficient quantity of soil has been eroded. The corresponding soil thickness is to be interpreted as a characteristic length scale  $S$  for which the medium can be considered homogeneous in terms of erosion resistance. This length is either a correlation scale of the intrinsic characteristics for a cohesive soil or simply the size of a grain for a sandy soil or. In practice, the cumulative amount of eroded soil is recorded with time for each couple of hydraulic shear stress and soil resistance on an elementary surface  $dA$ . When the specific eroded mass  $m_i/dA = \varepsilon_i \Delta t$  (with  $\Delta t$  the elapsed time from the last critical shear stress drawn  $(\tau_c)_i$ ) reaches the characteristic length  $S$ , we consider that the particles at surface exposed to erosion have been completely renewed. For these new particles initially deeper in the soil and coming to the surface, a new critical shear-stress is drawn into the distribution while the hydraulic shear stress  $\tau_i$  remains unchanged.

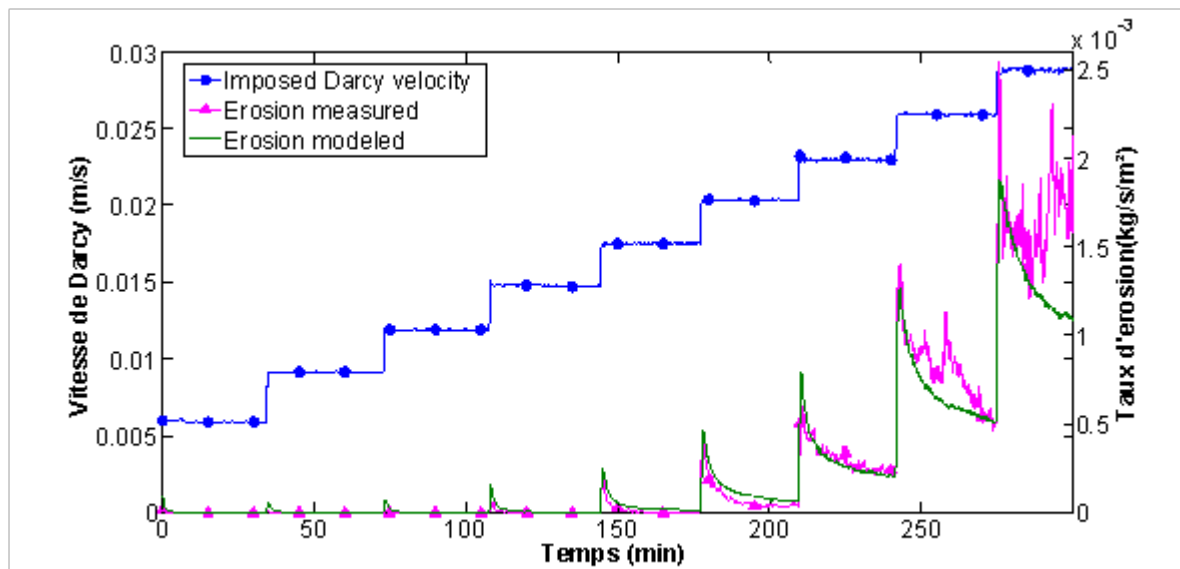


**Fig.13** : Time evolution of Darcy velocity and erosion rates measured during contact erosion tests (Guidoux, 2010) and erosion rate given by the stochastic model.

### c) Application of the model to contact erosion results

Guidoux et al., (2010) have carried out several contact erosion laboratory experiments on a silty-sand layer below a gravel layer. During these tests, the Darcy velocity in the gravel layers was increased by 30 min steps until contact erosion was generated at the interface of the two layers. The fine particles eroded were transported into the gravel and quantified at the exit by a turbidimeter. Typical evolutions with time of the mean hydraulic loading, Darcy velocity here, and of the erosion rate (estimated from the turbidity) are for instance the curves plotted in Fig.13. The model just presented in previous section 4.c has been tested on this particular set of data. The mean hydraulic shear-stress exerted on the fine soil layer is given by  $\langle \tau \rangle = \beta_i \beta_w \tau_w$  where  $\tau_w$  is calculated with equation (5) (Wörman, 1992), and with the rather strong assumption that the values of  $\beta_i$  and  $\beta_w$  obtained in our small-scale experiments (see section 3) can be used in this new configuration. Otherwise, different empirical values should be introduced. An exponential distribution is used for the probability density function according to equation (8). In term of soil resistance, the critical shear-stress distribution is chosen normal, as expressed in equation (11), with a mean value equal to the critical shear stress estimated thanks to Shields curve for the silt layer used in the experiments with  $d_{50}=60\mu\text{m}$ :  $\langle \tau_c \rangle = 0.12 Pa$ . The characteristic length scale  $S$  of the fine soil, defining the quantity of soil to erode before renewal of the fines particles at the surface, has been taken equal to the  $d_{50}$  of the fine soil which is granular. Finally, only the standard deviation of critical shear stress distribution and the coefficient of erosion have been used as free parameters of the model. The best agreement between the model prediction and the experimental data is obtained respectively for  $\sigma_{\tau_c} = 0.20 Pa$  and  $k_{er} = 6.8 \times 10^{-2} s/m$ . As can be seen in Fig.13, the model agrees quite well with the measurements obtained. The “peaks” of turbidity are well represented, as well as the subsequent exponential-like decreases of erosion with time.

So, the existence of these brief turbidity peaks, even for low mean velocity, can indeed be explained by high shear-stress values at a few places that can exceed locally the critical shear-stress. As the soil gets eroded in these few preferential starting points, the weakest particles are progressively extracted until this particular spot of erosion stops when all the remaining particles have a resistance higher than the hydraulic loading. As the mean velocity increases at each step increase, the locations with positive excess shear-stress become more numerous, and the hardening process less effective. This transition is similar to what was observed for free-surface fine soil erosion and called transition from type I to type II erosion (Parchure and Metha, 1985). But, here, the effect is enhanced by the specific hydraulic loading of contact erosion which exhibits a high spatial variability.

Decrease of erosion rate with time is also enhanced in the particular case of contact erosion by a potential clogging of the fine eroded particles in the pores of the coarse soil in contact. Indeed, one location of erosion is associated with one pore of the coarse layer, linked by different constrictions to several neighboring pores. If, during the erosion process, a particle larger than the constriction size is eroded and transported, it may clog the constriction

and block up this location for erosion. This phenomenon will tend to decrease the erosion rate with time and could be possibly added to the proposed model.

## Conclusion

Contact erosion is a common problem of internal erosion in river dikes or embankment dams, which can cause serious disturbances to the safety of these structures. Existing relationships to model this phenomenon are based on the classic sediment erosion in free surface flows with an empirical adjustment to account for the specificity of the hydraulic loading. Indeed, in contact erosion, the configuration to be considered is a porous flow along an interface between two soil layers with a sharp contrast in particle sizes.

The first objective of this paper was to characterize the specific hydraulic loading which generates contact erosion. For this purpose, an experimental device has been successfully implemented and allows for flow measurement by Particle Image Velocimetry in a refractive index matched medium composed of glass beads and oil. Measures that result are 2D velocity fields across the pore network and near a sand interface where erosion can occur. Probability density functions of velocity were obtained for longitudinal and transverse components. They are consistent with several literature data from numerical simulations and experimental measurements. Shear stresses fields were also deduced from the velocity fields, with particular attention near the solid-liquid interfaces where the PIV method has some limitations. To overcome this difficulty, a Poiseuille-like adjustment of the velocity measurement was used and extrapolated to the interface, providing a reliable value of shear stress at the surface. Knowledge of the shear stress on the soil surface exposed to erosion is critical because it is this quantity that is commonly used to quantify the erosion process. Again, the probability density functions have been calculated and show a behavior similar to longitudinal velocity distribution with an exponential-like trend of the tail. These distributions of velocity and shear-stress with this long tail of the distribution towards high values point to the strong spatial variability of liquid flows in a porous. This has important implications for the erosion process since, even at a low mean velocity of the flow, it exist local areas where shear stresses and velocities are high. For illustration, in our measurements, an interfacial shear stress three times higher than the average is found with a 5% probability, which is far from negligible.

Second, the mean shear stresses values measured at the solid-liquid interfaces were compared with various analytical formulas proposed in the literature. There is a significant difference between the analytical prediction and the measured value, but also a gap of about two between the measured mean shear stress in the porous bulk and the smaller one obtained at the interface of the sand layer. Two empirical coefficients are introduced to account for these effects

Finally, the distribution of hydraulic stresses identified above was used as the main ingredient in a stochastic model of contact erosion. Using a stochastic model provides an opportunity to also take into account the variability of soil resistance and time effect. Indeed, experimental tests at a larger scale with reconstituted soils have underlined that contact erosion is initiated by peaks which subsequently decrease with time (Guidoux, 2010). This is interpreted as an erosion of type I in the terminology consecrated for an open channel flow

(Parchure and Metha, 1985): the weakest particles are preferentially eroded and it follows a progressive hardening of the soil surface. To model this, a new value of the local resistance to erosion is drawn at random in all areas where a sufficiently large quantity of soil has been eroded. This conceptual model provides results consistent with the experimental data and is a promising step towards a more physical modeling of the erosion of contact.

## References

- Ariathurai, R. & Arulanandan, K. (1978), 'Erosion rates of cohesive soils', *Journal of the Hydraulics Division, ASCE* **104**(2), 279-283.
- Bakker, K. J.; Verheij, H. J. & de Groot, M. B. (1994), 'Design Relationship for Filters in Bed Protection', *Journal of Hydraulic Engineering* **120**(9), 1082-1088.
- Bear, J. (1972), *Dynamics of Fluids in Porous Media*, American Elsevier.
- Beguin, R. (2011), 'Etude multi-échelle de l'érosion de contact au sein des ouvrages hydrauliques en terre', PhD Thesis, Université de Grenoble, France.
- Bonelli, S. & Brivois, O. (2008), 'The scaling law in the hole erosion test with a constant pressure drop', *International Journal for Numerical and Analytical Methods in Geomechanics* **32**(13), 1573-1595.
- Brauns, J. (1985), 'Erosionsverhalten geschichteten Bodens bei horizontaler Durchströmung', *Wasserwirtschaft* **75**, 448-453.
- Cenedese, A. & Viotti, P. (1996), 'Lagrangian Analysis of Nonreactive Pollutant Dispersion in Porous Media by Means of the Particle Image Velocimetry Technique', *Water Resour. Res.* **32**(8), 2329--2343.
- Cheng, N.-S. (2006), 'Influence of shear stress fluctuation on bed particle mobility', *Physics of Fluids* **18**(9), 096602.
- Cheng, N.-S.; Law, A. W.-K. & Lim, S. Y. (2003), 'Probability distribution of bed particle instability', *Advances in Water Resources* **26**(4), 427 - 433.
- Den-Adel, H. & Bakker, M. A. K. K. (1994), 'The analysis of relaxed criteria for erosion-control filters', *Canadian Geotechnical Journal* **31**(6), 829-840.
- Duan, J. G. & Barkdoll, B. D. (2008), 'Surface-Based Fractional Transport Predictor: Deterministic or Stochastic', *Journal of Hydraulic Engineering* **134**(3), 350-353.
- Giese, M.; Rottschäfer, K. & Vortmeyer, D. (1998), 'Measured and modeled superficial flow profiles in packed beds with liquid flow', *AIChE Journal* **44**(2), 484--490.
- Guidoux, C.; Faure, Y.-H.; Beguin, R. & Ho, C.-C. (2010), 'Contact Erosion at the Interface between Granular Coarse Soil and Various Base Soils under Tangential Flow Condition', *Journal of Geotechnical and Geoenvironmental Engineering* **136**(5), 741-750.
- Hlushkou, D. & Tallarek, U. (2006), 'Transition from creeping via viscous-inertial to turbulent flow in fixed beds', *Journal of Chromatography A* **1126**(1-2), 70 - 85.
- Huang, A.; Huang, M.; Capart, H. & Chen, R.-H. (2008), 'Optical measurements of pore geometry and fluid velocity in a bed of irregularly packed spheres', *Experiments in Fluids* **45**, 309-321.
- Hunziker, R. P. & Jaeggi, M. N. R. (2002), 'Grain Sorting Processes', *Journal of Hydraulic Engineering* **128**(12), 1060-1068.



- Johns, M. L.; Sederman, A. J.; Bramley, A. S.; Gladden, L. F. & Alexander, P. (2000), 'Local transitions in flow phenomena through packed beds identified by MRI', *AIChE Journal* **46**(11), 2151--2161.
- Knapen, A.; Poesen, J.; Govers, G.; Gyssels, G. & Nachtergaele, J. (2007), 'Resistance of soils to concentrated flow erosion: A review', *Earth-Science Reviews* **80**(1-2), 75--109.
- Lachhab, A.; Zhang, Y.-K. & Muste, M. V. (2008), 'Particle Tracking Experiments in Match-Index-Refractive Porous Media', *Ground Water* **46**(6), 865--872.
- Lavelle, J. W. & Mofjeld, H. O. (1987), 'Do Critical Stresses for Incipient Motion and Erosion Really Exist?', *Journal of Hydraulic Engineering* **113**(3), 370-385.
- Lebon, L.; Leblond, J.; Hulin, J.-P.; Marty, N. & Schwartz, L. (1996), 'Pulsed field gradient NMR measurements of probability distribution of displacement under flow in sphere packings', *Magn Reson Imaging* **14**(7), 989--991.
- Locke, M.; Indraratna, B. & Adikari, G. (2001), 'Time-Dependent Particle Transport through Granular Filters', *Journal of Geotechnical and Geoenvironmental Engineering* **127**(6), 521-529.
- Magnico, P. (2003), 'Hydrodynamic and transport properties of packed beds in small tube-to-sphere diameter ratio: pore scale simulation using an Eulerian and a Lagrangian approach', *Chemical Engineering Science* **58**(22), 5005 - 5024.
- Maier, R. S.; Kroll, D. M.; Davis, H. T. & Bernard, R. S. (1999), 'Simulation of Flow in Bidisperse Sphere Packings', *Journal of Colloid and Interface Science* **217**(2), 341 - 347.
- Meunier, P. & Lewke, T. (2003), 'Analysis and treatment of errors due to high velocity gradients in particle image velocimetry', *Experiments in Fluids* **35**, 408-421.
- Parchure, T. M. & Mehta, A. J. (1985), 'Erosion of Soft Cohesive Sediment Deposits', *Journal of Hydraulic Engineering* **111**(10), 1308-1326.
- Rashidi, M.; Peurrung, L.; Tompson, A. F. B. & Kulp, T. J. (1996), 'Experimental analysis of pore-scale flow and transport in porous media', *Advances in Water Resources* **19**(3), 163 - 180.
- Reboul, N.; Vincens, E. & Cambou, B. (2010), 'A computational procedure to assess the distribution of constriction sizes for an assembly of spheres', *Computers and Geotechnics* **37**(1-2), 195 - 206.
- Reddi, L. N.; Lee, I.-M. & Bonala, M. V. S. (2000), 'Comparison of internal and surface erosion using flow pump tests on a sand-kaolinite mixture', *ASTM geotechnical testing journal* **23**(1), 116-122.
- Sherard, J. L.; Dunnigan, L. P. & Talbot, J. R. (1984), 'Basic Properties of Sand and Gravel Filters', *Journal of Geotechnical Engineering* **110**(6), 684-700.
- Valyrakis, M.; Diplas, P.; Dancy, C. L.; Greer, K. & Celik, A. O. (2010), 'Role of instantaneous force magnitude and duration on particle entrainment', *J. Geophys. Res.* **115**(F2), F02006--.
- Van Prooijen, B. C. & Winterwerp, J. C. (2010), 'A stochastic formulation for erosion of cohesive sediments', *J. Geophys. Res.* **115**(C1), C01005--.
- Wörman, A. & Olafsdottir, R. (1992), 'Erosion in a granular medium interface', *Journal of Hydraulic Research* **30**(5), 639-655.